Dudamell, N.V.; Ulacia, I.; Galvez, F.; Yi, S.; Bohlen, J.; Letzig, D.; Hurtado, I.; Perez-Prado, M.T.:

Twinning and grain subdivision during dynamic deformation of a Mg AZ31 sheet alloy at room temperature

In: Acta Materialia (2011) Elsevier

DOI: 10.1016/j.actamat.2011.07.047

Twinning and grain subdivision during dynamic deformation of a Mg AZ31 sheet alloy at room temperature

N. V. Dudamell[1], I. Ulacia[2], F. Gálvez[3], S. Yi[4], J. Bohlen[4], D. Letzig[4], I. Hurtado[2], M.T. Pérez-Prado[1,*]

[1]*Madrid Institute for Advanced Studies in Materials, IMDEA Materials, 28040 Madrid, Spain*
[2]*Mondragon Goi Eskola Politeknikoa, Mondragon Unibertsitatea, 20500 Mondragón, Spain*
[3]*ETS Ingenieros de Caminos, Universidad Politécnica de Madrid, 28040 Madrid, Spain*
[4]*Magnesium Innovation Center, Helmholtz-Zentrum Geesthacht, 21502 Geesthacht, Germany*
** Corresponding author*

Abstract

Keywords: Magnesium, AZ31, High strain rate, Twinning, Slip, Grain subdivision.

The microstructural evolution of an AZ31 rolled sheet during dynamic deformation at strain rates of ~10^3 s^{-1} has been investigated by electron backscatter diffraction, X-ray and neutron diffraction. The influence of orientation on the predominant deformation mechanisms as well as on the recovery processes taking place during deformation has been systematically examined. The results have been compared with those corresponding to the same alloy tested quasi-statically under equivalent conditions. It has been found that strain rate enhances dramatically the activation of {$\bar{1}$or2} extension twinning, while contraction and secondary twinning are not significantly influenced. The polarity of {$\bar{1}$or2} extension twinning is even reversed in some grains under selected testing conditions. Significant grain subdivision by the formation of geometrically necessary boundaries (GNBs) takes place during both quasi-static and dynamic deformation of this AZ31 alloy. It is remarkable that GNBs of high misorientations form even at the highest strain rates. The phenomenon of recovery has been found to be orientation dependent.

1. Introduction.

Magnesium alloys are light metals (ρ~1.7 g/cm^3) that have been profusely studied over the last decade due to their potential in the transportation and aerospace industries, among others [1-3]. The deformation and dynamic recrystallization mechanisms of Mg alloys at low strain rates are nowadays well known [4-33]. Slip may take place along the <$1\bar{1}$0> (<a>) direction on basal and non-basal ({$10\bar{1}$0}-prismatic, {$10\bar{1}$1}-pyramidal) planes. Additionally, <c+a> slip has also been observed along {$11\bar{2}$2} second order pyramidal planes [22]. The predominance of a specific slip system is dependent on the deformation temperature, as well as on the crystallographic texture [4-33].

Twinning, mainly on {$10\bar{1}$2}, {$10\bar{1}$1} and {$10\bar{1}$3} planes, plays a key role during deformation of Mg alloys, particularly at low temperatures [8,13,16,19,22,33]. Twinning is a polar mechanism [34]. For example, extension twinning in {10-12} planes is active in a grain only when the deformation conditions are such that an extension along the c-axis takes place [26]. This mechanism is especially important in strongly textured wrought Mg alloys. It is well known that rolled Mg sheets have a strong basal-type texture (the c-axes are parallel to the normal direction, ND), and thus extension twinning is the predominant deformation mechanism during the first stages of deformation when compressive loading is applied in a direction parallel to the rolling plane. In extruded Mg rods, in which the c-axes align with the radial directions during processing, extension twinning predominates when a compressive stress is applied in the extrusion direction. In both cases twinning leads to a reorientation of the lattice of 86° in such a way that, after about 4-6% of strain, the c-axes of *most* grains become parallel to the applied stress. Tensile twinning is favored at high strain rates and low temperatures [34]. In randomly oriented polycrystals basal slip and {$10\bar{1}$2} twinning are

the predominating deformation mechanisms in selected grains, that are favorably oriented for this deformation mode.

When the c-axis of a Mg grain is placed under compression, both contraction twinning and non-basal slip might be activated. Twinning under such conditions takes place mostly in $\{10\bar{1}1\}$ planes, causing a lattice reorientation of approximately 56° around the <11-20> axis. Occasionally, areas that have undergone contraction twinning are in a suitable orientation for subsequent extension twinning. The consecutive occurrence of these two twinning mechanisms gives rise to the so-called secondary twinning mechanism [35]. The misorientation angle of the twin boundary surrounding a secondary-twinned area is approximately 38° around the <11-20> axis. The significance of contraction and secondary twinning in accommodating c-axis compression in magnesium alloys is still not clear. In fact, the experimental evidence available suggests that their net contribution to the total deformation is not very significant. In particular, contraction and secondary twinning have been claimed to operate in Mg single crystals tested with the tensile axis parallel to the basal plane [36-38]. However, single crystal studies were carried out several decades ago and rely mostly on optical microscopy. Furthermore, traces of these mechanisms have only been found in very localized regions (e.g., close to the fracture surface or to the sample surface itself). Finally, the ductilities of these single crystals rarely exceed 2%, and thus it remains unclear from these experiments whether these mechanisms can be responsible for the larger fracture strains typically observed in Mg polycrystals. Some studies have recently reported the occurrence of contraction and secondary twinning in polycrystalline Mg alloys during c-axis compression [24,28,39-41]. However, again, traces of these types of twins are only observed in very small regions, often very close to the fracture surfaces. Thus, it is now widely accepted that pyramidal slip accommodates most of the compression strain along

the c-axis [16,42]. Some authors have highlighted the role of compression twins in the strain hardening of Mg alloys [42].

While twinning in Mg alloys at quasi-static strain rates has been extensively studied, the occurrence of this mechanism at dynamic strain rates has still not been thoroughly explored. It is known that, in this strain rate range, twinning is active even at temperatures as high as 400°C [43-47], at which it is mostly suppressed at quasi-static strain rates. However, the effect of strain rate on the activity of the different twinning modes is still unknown.

In a recent study [43] the present authors have analyzed in detail the mechanical response of the Mg alloy AZ31 under dynamic loading conditions. In particular, the temperature dependencies of the tension-compression yield asymmetry, the yield strength anisotropy and the CRSS of the various slip systems at those high strain rates were thoroughly investigated. However, the microstructural evolution of Mg alloys with strain under dynamic conditions and, more specifically, the dependence, if any, of the grain size, grain boundary distributions and restoration mechanisms on the straining direction have still not been studied.

In this work we describe the microstructure and microtexture evolution of a Mg AZ31 rolled sheet during dynamic deformation at room temperature as a function of the strain and of the orientation of the applied stress. In particular, the conditions analyzed include compression along the rolling and normal directions (RD and ND) and tension along RD. Special attention is paid to the evolution of the grain boundary distributions, which give very valuable information regarding the presence of any restoration mechanisms, and to the activity of the various twinning modes. The room temperature microstructural evolution of this rolled Mg AZ31 alloy at high strain rates is compared to that taking place at quasi-static strain rates.

2. Experimental procedure.

2.1 Material: initial microstructure.

The material under study is the Mg alloy AZ31. Two rolled and annealed sheets, 1 and 3 mm in thickness, were purchased from Magnesium Elektron. The initial microstructures of the two AZ31 sheets consist of equiaxed grains, with average sizes of 10 and 13 μm, respectively. As generally observed in annealed AZ31 sheets, both have a characteristic strong basal-type texture with a spread of the (0001) poles toward the RD. In the following we will refer to both sheets as "the AZ31 alloy", as their microstructure and mechanical behavior are basically identical. Further considerations about the similarity of the two materials can be found in [43].

2.2 Mechanical testing.

Room temperature high strain rate ($\dot{\varepsilon}\sim10^3$ s^{-1}) mechanical tests were performed in the AZ31 alloy up to failure and up to several intermediate strains using a Hopkinson bar furnished with a high speed camera. The specimens were dynamically loaded to a predefined strain level, using a stop-ring technique which limits the displacement of the incident Hopkinson bar. Ring stoppers of specific heights were machined out of an F522 steel.

Compression tests along RD were performed in 3x3x4.5 mm specimens and compression tests along ND were carried out in 3x3x3 mm cubes. Tensile tests along RD were performed in dog-bone shaped tensile specimens with a gage length of 12.5 mm and a width of 1.75 mm. The reader is referred to [48] for a more detailed description of the testing procedures.

Quasi-static tests at a strain rate of 10^{-3} s^{-1} were also carried out until failure and up to some intermediate strains along the same directions described above in order to compare the variations in the microstructural evolution with the strain rate. These tests

were carried out in a conventional universal testing machine (Instron) using the same specimen geometries described above. For the tension tests along RD the specimens were machined following the ASTM E8M-00 standard with a gage length of 32 mm and a width of 6 mm.

2.3 Microstructure examination.

The microstructure and the texture of a number of samples compressed along RD and ND and tensile tested along RD at room temperature up to various strain levels were analyzed by electron backscatter diffraction (EBSD) using the TSL-OIM^{TM} software in a Zeiss Ultra 55^{TM} FEG-SEM. Sample preparation for EBSD investigations included grinding with 4000 SiC paper, mechanical polishing with a 0.05 μm silica suspension and final electro-chemical polishing for 90 s at 33 V using the AC2^{TM} commercial electrolyte. The microstructure is represented by EBSD orientation maps and the texture by pole figures recalculated from the EBSD orientation data. In order to investigate the operative deformation and restoration mechanisms, the nature of the grain boundaries present in all the samples was analyzed from the EBSD data. Special attention was paid to the presence of twin boundaries and to the misorientation distribution histograms. Additionally, the grain size of various samples was calculated by the linear intercept method in the EBSD orientation maps using only grain boundaries with misorientations higher than 15°.

Since EBSD only allows examining the local texture, macrotexture measurements were also performed in selected samples by neutron diffraction at the STRESS-SPEC instrument at the research reactor FRM II, Munich Technical University, Germany. The area examined had a diameter of approximately 5 mm. A Ge monochromator with an associated wavelength of 1.65Å was used. The macrotexture of some samples was also measured by the Schulz reflection method in a Philips X´pert-Pro Panalytical X-ray

diffractometer furnished with a PW3050/60 goniometer, located at the CAI X-rayDiffraction of the University Complutense in Madrid, Spain. The radiation used was β-filtered Cu Kα. The surface area examined was about 2mm^2. The polar angle ranged from 0° to 75° in steps of 3°. Irradiation time at each step was 2s. The measured incomplete pole figures were corrected for background and defocusing using the Philips X´pert software. The orientation distribution function (ODF) and the complete pole figures were calculated using the MTex software [49]. Sample preparation for texture measurement included grinding with increasingly finer SiC papers, whose grit size ranged from 320 to 2000.

3. Results.

3.1 Mechanical behavior.

Figure 1 illustrates the stress-strain curves corresponding to room temperature tests carried out until failure under compression along RD (Fig. 1a), tension along RD (Fig. 1b), and compression along ND (Fig. 1c). Tests carried out at dynamic rates (10^3 s^{-1}) and under quasi-static conditions ($5x10^{-3}$ s^{-1} in the compression tests and 10^{-3} s^{-1} in the tension test) are compared. Images illustrating the three tested samples after macroscopic fracture (i.e., after the complete test) under dynamic conditions, captured in-situ by a high speed camera, have been added to the corresponding stress-strain curves. These images show the resulting adiabatic shear failure, a dynamic fracture mechanism that develops in the vast majority of ductile materials subjected to impact loading. Adiabatic shear bands (ASB) are regions in which very high local strains and very high temperatures develop, leading to uncontrolled failure [50]. At strains lower than those at which ASBs form, homogeneous deformation takes place throughout the specimen; at higher strains the deformation is highly localized in the bands, the rest of

the material remaining basically in the deformation state corresponding to the instant prior to localization.

The occurrence of ASBs in dynamically deformed materials has been extensively investigated [50, 51]. The classical model for the prediction of the onset of ASB formation (Zener-Hollomon) [52] relies on the competition between strain hardening and thermal softening of the material, and it predicts that the onset of the bands coincides with the strain at which the material loses its hardening capacity. The curves corresponding to the dynamic compression tests along RD and ND (Figs. 1a and 1c) show significant strain hardening followed by pronounced softening. The curve corresponding to dynamic tension along RD (Fig. 1b) also shows the presence of work hardening followed by some softening, albeit to a lesser extent than in the other two cases investigated. According to the Zener-Hollomon criterion the strains, ε_f, at which ASBs form during the three tests investigated here (compression along RD, Fig. 1a, tension along RD, Fig. 1b, and compression along ND, Fig. 1c) would be 0.16, 0.18, and 0.07, respectively. These strains are pointed out with arrows in Fig. 1. The dynamic fracture energies for the three tests are 3.9×10^7 J/m^3, 4.8×10^7 J/m^3, and 2.2×10^7 J/m^3, respectively. These values are clearly dependent on the test mode (tension vs. compression) and on the loading direction with respect to the c-axes of the polycrystalline aggregate, as different deformation mechanisms are activated in each of the three tests investigated. Rittel et al. [53] suggested that the onset of ASBs could start at lower strains than those predicted by the Zener-Hollomon model, since in their view ASBs form by early dynamic recrystallization before ε_f. Determining the exact strain at which ASB formation starts would, then, require a thorough investigation by transmission electron microscopy which is out of the scope of the present paper and it would constitute a separate study by itself. Since we are interested in analyzing the

dynamic deformation mechanisms during *homogeneous* deformation of the AZ31 alloy, we will consider that, as long as clear bulk microstructural changes take place in the specimen with straining, we will be examining samples deformed to strains lower than those required for ASB formation since, once ASBs form, strain localization in these narrow regions leads to the "freezing" of the microstructure elsewhere. During homogeneous dynamic straining the temperature rise during testing is lower than about 30 K [53].

It can be seen in Fig. 1 that dynamic tests exhibit higher flow stresses than the corresponding quasi-static tests. The elongations to failure, ε_f, are basically comparable in both strain rate regimes. In compression, ε_f, is slightly higher under dynamic conditions. The differences in the mechanical behavior with strain rate will be rationalized on the light of the microstructural evolution during testing, which will be described in the following section.

3.2 Microstructural evolution.

Each of the three dynamic tests investigated was carried out to failure (Fig. 1) and also stopped at various intermediate true strains in order to analyze the microstructure evolution of the AZ31 alloy under high strain rate conditions. In compression along RD (Fig. 1a) tests were interrupted at strains of 0.05, 0.10, and 0.13. All of these strain values are lower than ε_f (0.16), the value at which ASBs form according to the Zener-Hollomon criterion [51]. In tension along RD (Fig. 1b), tests were stopped at strains of 0.10 and 0.20. The latter value is higher than ε_f (0.18), indicating than the homogeneous strain accumulated in this sample will be lower than 0.20, as shear localization takes place at lower strains. The compression tests along ND (Fig. 1c) were stopped at strains of 0.05 and 0.10. Again, the latter is higher than the corresponding ε_f (0.07), and

therefore it is expected that the homogeneous strain accumulated in this sample is lower than 0.10.

3.2.1 Compression along RD.

Figure 2 illustrates the EBSD inverse pole figure maps in the ND and the microtextures of the samples deformed at $5x10^{-3}$ s^{-1} in compression along RD up to strains of 0.05 and 0.13. As is well known [21,26,43], extension twinning takes place during the first stages of deformation (Fig. 2a), leading to an 86° rotation of the c-axes which brings them into alignment with RD (compression axis). A single texture component develops, with <$1_{or}0$> directions parallel to ND (Fig. 2a). Extension twins nucleate and propagate quickly, often encompassing the entire grain [42]. The area fraction of extension twinned material at a strain of 0.05 is 68% and it increases up to 85% at a strain of 0.13 (Fig. 2b). The volume fraction, estimated from X-ray ODF measurements, is approximately 72% at a strain of 0.13. These values are consistent with previous studies [54]. A significant fraction of extension twin boundaries, plotted in red in Fig. 2c, are thus still present in the microstructure even at the largest strains investigated here. Contraction and secondary twins, plotted in green and yellow in Fig. 2c, are basically absent. The grain size, measured counting only high angle boundaries (misorientation, θ, > 15°), including twin boundaries, is equal to 6 μm at a strain of 0.05 and to 8.5 μm at a strain of 0.13. The reduction in grain size (from a value of 13 μm in the as-received material) is mainly attributed to the presence of the twin boundaries. In the twinned grains pyramidal slip becomes the dominant deformation mechanism, together with basal slip [21,43]. The single component texture described above is retained until failure. Grain subdivision by the formation of geometrically necessary boundaries takes place as well during the last stages of deformation. It can be seen in Fig. 2c that newly

formed boundaries, lying perpendicular to the compression axis, traverse the original grains. Some of these new boundaries are pointed with white arrows.

Figure 3a-c illustrates the EBSD inverse pole figure maps in the ND and the microtextures of the samples deformed at high strain rate (~10^3 s^{-1}) in compression along RD up to strains of 0.05, 0.10, and 0.13. These three strains are included within the hardening region of the stress-strain curve. A clear microstructural evolution with strain can be observed. Significant extension twinning activity takes place at the early stages of deformation. At ε=0.05 the fraction of twinned material, calculated from the EBSD data, is 81% (compare with 68% at low strain rates) and the grain size is 9 μm (compare with 6 μm at low strain rate). Together, these data reveal that the nucleation and propagation of extension twins is significantly enhanced at dynamic strain rates. Twinning at high rates leads to the development of the same single component texture described above for quasi-static strain rates (<0001> directions parallel to RD and <$1_{or}0$> directions parallel to ND). The volume fraction of twinned material increases to 98% at ε=0.10. The texture intensity increases slightly from ε=0.05 to ε=0.10, due to the increase in the volume fraction of twins, and then it remains basically constant. This is consistent with the operation of pyramidal and basal slip during the last stages of deformation. The intragranular Kernel average misorientation (KAM) parameter increased from 1 at ε=0.05, to 1.3 at ε=0.10, and to 1.2 at ε=0.13, consistently with the higher slip activity at the later stages of deformation.

Fig. 3d presents the EBSD boundary map of the sample deformed to ε = 0.13. It can be clearly appreciated that grain subdivision by the formation of geometrically necessary boundaries (GNBs) has taken place. We have observed that low to medium angle boundaries, lying mostly perpendicular to the applied stress, start in fact forming already at the early stages of deformation (ε=0.05) by dislocation accumulation in the

twinned grains, where crystallographic slip takes place. With increasing strain, the misorientation of these boundaries increases, leading ultimately to high angle boundaries. Some examples of boundaries transitioning from low to moderate misorientation angle and, from the latter, to becoming high angle boundaries, are pointed with arrows in Fig. 3d. Further evidence of this phenomenon can be found in Fig. 4, which illustrates the misorientation distribution histograms corresponding to the samples deformed up to ε=0.05, 0.10, and 0.13. Boundaries with θ>5° are included. It can be clearly appreciated that extension twin boundaries (θ=86°) are predominant a low strains and that the fraction of boundaries with misorientations between 5° and 50° increase with strain. As a result, the grain size remains basically constant until failure (d=9.5 μm at ε=0.10 and d=10 μm at ε=0.13). The grain size corresponding to the sample deformed at low strain rate up to ε=0.13 is 8.5 μm. This difference can be attributed to the higher fraction of twin boundaries in the latter. We could not detect any significant differences in the process of grain subdivision between samples deformed at low and high strain rates (Figs. 2 and 3).

The above results allow explaining the differences in the mechanical behavior of this AZ31 alloy at low and high strain rates under compression along RD (Fig. 1a). First, since the CRSS of twinning is strain-rate independent [43], both samples yield at approximately the same stress level and during the first stages of deformation (ε < 0.03) exhibit similar hardening rates. However, extension twins propagate faster at high strain rate and thus crystallographic slip (pyramidal and basal) becomes the predominant deformation mechanism at small strains (~0.03). Since the CRSS of pyramidal slip is higher than that of twinning at room temperature [43], at a strain of, for example, 0.05, the flow stress is higher in the sample that is dynamically deformed. For ε > 0.03 the hardening rate in samples deformed dynamically corresponds mainly to dislocation-

dislocation interactions, as very few twin boundaries remain present. In contrast, in the low strain rate regime crystallographic slip becomes predominant at higher strains (~0.06). Since the volume fraction of twinned areas saturates at a value in the range of 72%-85%, the amount of twin boundaries that remains present is larger than in the microstructure deformed at high strain rate. Thus, the hardening rate is higher than in the dynamic case due to the presence of dislocation-twin boundaries interactions, in addition to the dislocation-dislocation interactions.

3.2.2 Tension along RD.

It is well known that, at low strain rate, deformation in tension along RD takes place mainly by prismatic slip, together with basal slip [22,24,33,43]. Figure 5 shows the pole figures, measured by neutron diffraction in order to get a good statistical description of the macrotexture, corresponding to the AZ31 alloy deformed at 10^{-3} s^{-1} up to failure. With increasing deformation, a single component texture develops, in which c-axes remain mostly parallel to ND and <$1_{or}0$> directions become aligned with the tensile axis (RD).

Figure 6 illustrates the EBSD inverse pole figure maps in the ND and the direct pole figures, measured by neutron diffraction, corresponding to the AZ31 alloy deformed dynamically in tension along RD. Data corresponding to strains of 0.10 (Fig. 6a) and 0.20 (Fig. 6b) are presented. It has to be pointed out that, as explained in detail in section 3.1, the onset of adiabatic shear banding takes place at a strain of 0.18. Therefore, the true *homogeneous* strain accumulated in this sample is smaller than this value. A clear evolution of the microstructure can be observed in the two samples investigated. First, the same deformation texture described above for quasi-static tests (<0001> directions parallel to ND and <$1_{or}0$> directions aligned with the tensile axis (RD), develops during dynamic straining. The intensity of this texture has been found to

be similar at dynamic and quasi-static rates (Figs. 5 and 6). Second, an additional intensity maximum can be detected, which reveals the alignment of c-axes perpendicular to the tensile axis (parallel to TD). This component is associated with extension twinning. Its intensity increases with strain. We are showing neutron diffraction pole figures in order to prove that the presence of extension twins is an important contributor to deformation, and not merely an accommodation mechanism, as has been suggested for low strain rate deformation under the same conditions [16]. Extension twinning is, thus, clearly enhanced at high strain rates, taking place in grains that would otherwise not be suitably oriented for the activation of this mechanism at low strain rates. Once formed, extension twins are stable under this loading condition, as they are not favorably oriented either for de-twinning or for basal slip. They, thus, must deform by non-basal slip, as the rest of the material.

Figure 6c shows the twin boundary map corresponding to the sample deformed to a strain of 0.20. A significant fraction of extension twin boundaries are indeed present. It must be noted that extension twin boundaries are not straight, as is commonly observed. Instead, their morphology is very wavy (see arrows in Fig. 6c), revealing that twin boundary propagation is sluggish under the current deformation conditions. This is not surprising since extension twinning is somehow "forced" in grains that would otherwise not twin at low strain rate, presumably by the large amount of energy accumulated during impact loading.

Figure 7 illustrates the boundary maps corresponding to the AZ31 alloy deformed at high strain rate up to strains of 0.10 (Fig. 7a) and 0.20 (Fig. 7b), and at low strain rate up to failure (the strain is approximately 0.23) (Fig. 7c). Fig. 7d shows the twin boundary map corresponding to the low strain rate sample. It can be seen, first, that the amount of low to medium angle boundaries (red and green in Fig. 7a and 7b), formed

by dislocation interactions, increases with strain during dynamic deformation. Second, the grain size, measured counting only high angle boundaries, decreases from 10 μm in the initial material to 7.1 μm at a dynamic strain of 0.10 (Fig. 7a) and to 7.2 μm at a dynamic strain of 0.20 (Fig. 7b). This decrease is mainly attributed to the twin boundaries created during high strain rate deformation. Third, in the sample deformed at low strain rate (Figs. 7c and d) the grain size reduction is much more pronounced (d~ 2.5 μm). The presence of extension twins in this sample is significantly lower than at an equivalent dynamic strain (Fig. 6c), although it seems contraction and secondary twins are more abundant. However, the increase in contraction and secondary twin boundaries is not large enough to justify the significant decrease in grain size. Therefore, the significant decrease in grain size observed at low strain rates must be mainly attributed to a larger degree of grain subdivision by the formation of geometrically necessary boundaries. Our results, thus, suggest that this process of grain refinement is more pronounced at low strain rates.

If the curves of Fig. 1b are compared, it can be seen that the yield stress at dynamic rates is higher than at low strain rates. This can be attributed to the higher CRSS of prismatic systems at higher strain rates [43]. The hardening rate under dynamic conditions tends to remain constant or increase with strain, while at low strain rates it decreases gradually, as is commonly observed in polycrystalline materials [55]. This difference in the hardening behavior is attributed to the higher degree of recovery present at low strain rate, which results in the formation of a larger fraction of GNBs.

3.2.3 Compression along ND.

Under these conditions the predominant deformation mechanisms at low strain rates are pyramidal and basal slip [16,42]. Some compression twinning is also activated in localized regions.

Fig. 8 illustrates the EBSD inverse pole figure maps in the ND as well as the macrotexture (measured by X-ray diffraction) and the microtexture (EBSD) corresponding to the samples deformed at high strain rate up to strains of 0.05 (Fig. 8a) and 0.10 (Fig. 8c). The latter strain is higher than the Zener-Hollomon failure strain (0.07), which implies that the total homogeneous strain accumulated in the sample plotted in Fig. 8b is probably closer to 0.07 than to 0.10. Fig. 8b is the twin boundary map corresponding to Fig. 8a. Significant microstructural changes take place during dynamic straining. First, surprisingly, a large amount of extension twins are clearly visible after a strain of 0.05. The fraction of extension twinned area, calculated from EBSD data, is 17%. The presence of extension twinning is reflected in the intensity maximum that appears at orientations tilted 90° to the ND in the macro and micro (0001) direct pole figures of Fig. 8a. We have included the macrotexture in order to proof that the occurrence of extension twinning is not a local effect. It must be emphasized that these twins appear in grains that are unfavorably oriented for this mechanism to be activated, i.e., which have c-axes parallel to the compression axis. This is surprising as it is well known that twinning is a polar mechanism and that extension twins are only predicted to occur in grains in which an extension along the c-axis takes place. Our data confirm that the polarity of twinning is inverted in some grains under dynamic compression along ND. This is yet another evidence of how high strain rates stimulate *extension* twinning. We have not observed a similar effect for compression twins, which are scarce (Fig. 8b) despite most grains are oriented favorably for this mechanism to be activated. The extension twins formed are very soft regions in comparison with the remaining of the material, which has a basal texture. Thus, it is expected that, under compression along ND, de-twinning takes place. Indeed, both macro and microtexture data in Fig. 8c, reveal that extension twins revert back to their

original orientation (c-axes aligned with ND) at higher strains. EBSD (micro) pole figures show a preferential alignment of <$1\bar{0}10$> directions with TD after de-twinning, but this is considered a local effect, as macrotexture data suggest the presence of a perfect basal fiber.

The grain size after dynamic compression along ND up to a strain of 0.05 decreases from 13 μm (initial material) to 10 μm, due to the presence of the extension twin boundaries. With increasing deformation, after de-twinning, the grain size increases again, reaching a value of 16 μm. This high value suggests that no significant grain subdivision by the formation of geometrically necessary boundaries has taken place under these deformation conditions. This seems reasonable, as the strains investigated are significantly lower than those undergone by the samples deformed in compression and in tension along RD (sections 3.1.1 and 3.1.2).

The present results suggest that the increase in ductility with strain rate (Fig. 1c) might be due to the activation of additional deformation mechanisms, such as twinning and de-twinning. Finally, since the extension twins formed at intermediate strains are very soft regions, they might constitute favorable locations for the nucleation of adiabatic shear bands.

4. Discussion

4.1 Influence of strain rate on the twinning activity.

It is now well known that twinning is enhanced in Mg alloys during dynamic deformation to such an extent that it is present even at very high temperatures (400°C) [34,43-47], at which it is absent at low strain rates. A profuse twinning activity at dynamic rates has also been reported in other hcp metals, such as Ti and Zr [56-58]. Our current work additionally reveals that the influence of the strain rate on the AZ31 alloy

consists on the enhancement of extension twinning, but that compression and double twinning are, not only not enhanced, but even hindered under dynamic conditions. In particular, we have observed that strain rate enhances extension twin propagation in grains that are favorably oriented for this mechanism to operate, and that it promotes the nucleation of extension twins even in grains that would not be favorably oriented for extension twinning at low strain rates.

The enhancement of extension twinning at high strain rates can be rationalized as follows. Arguments based on variations of the critical resolved shear stress for twinning with strain rate must be ruled out, as it is well known that this parameter is strain-rate and temperature insensitive [19,34,43]. The choice of twin systems was classically based on the criterion of minimum shear put forward by Jaswon and Dove [59,34]. This model assumes that the atoms in the twinned area reach their final positions exclusively by pure shear, which excludes atomic translations (shuffles). The twinning shears associated to extension and compression twinning in Mg (s) are, respectively, -0.1289 and 0.1377 [34]. These values are very similar, but yet usually extension twins are abundant and thick, while the compression twins are often observed only in localized regions. Furthermore, this criterion does not explain why extension twinning is preferentially enhanced at high strain rates, since shear is not diffusion assisted. A more sophisticated model for determining the operative twin systems was proposed by Bilby and Crocker [60,34]. This model considers twinning as a combination of shear plus individual atomic shuffles. The latter are temperature and strain-rate dependent [61]. Bilby and Crocker suggested that the operative twin mode should, besides having a small shear, require only simple shuffles. The "simplicity" of the atomic shuffles is related in their theory to a positive integer parameter (q), associated to each twinning mode, which is the number of lattice invariant planes ($\mathbf{K_1}$)

of spacing *d* traversed by the primitive lattice vector in the shear direction (η_2) [34]. The lower the value of "q", the simpler the shuffles involved. For extension twinning q=4 while for $\{10\bar{1}1\}$ contraction twinning q=8 [34]. Thus, contraction twinning involves more complicated atom shuffling. Since atomic translations (shuffling) are activated thermally, an increase in the strain rate would hinder these atomic movements, even more so if they are complex. Therefore contraction twinning expected to be less favored than extension twinning at high strain rates. This is consistent with our observations.

The enhancement of extension twinning under dynamic conditions is especially dramatic during compression along ND, where the polarity of twinning is reversed in a rather large number of grains. It is remarkable that an inversion of the polarity of tensile twinning is preferred to an enhancement of compression twinning in grains in which the c-axes are being compressed. The reason for this surprising phenomenon is not entirely clear. Let us revise the concept of twin polarity. The shear associated to a specific twinning system (*s*) is calculated as the ratio between the modulus of the corresponding twinning dislocation (b_{TD}) and the step height, h ($s=b_{TD}/h$) [34]. For twinning modes with q higher than 2 and even, $s \sim 2b_{TD}/q$ [34]. b_{TD}, and therefore *s*, may also be expressed as a function of the c/a ratio (γ). For $\{10\bar{1}2\}$ twins, $s = (2b_{TD}/q) = (\gamma^2-3)/3^{1/2}\gamma$. The shear, thus, changes dramatically with the c/a ratio. In Mg, γ is equal to 1.624 and the resulting shear is negative. This makes this twinning mode a *tension twin* [9,34]. Within this framework, the observation of $\{10\bar{1}2\}$ twins during c-axes compression at dynamic rates implies that the associated twinning shear adopts a positive value. This could only be achieved if the c/a ratio would increase by approximately 5% during elastic deformation, which is not observed experimentally, or if a different mechanism (other than the propagation of the above mentioned twinning dislocation) would dominate $\{10\bar{1}2\}$ twinning under the mentioned conditions. Some

controversy does indeed exist regarding the fundamental mechanism responsible for $\{\bar{1}02\}$ twinning in Mg alloys [62,63].

4.2 Influence of strain rate on dynamic recovery.

It is well known that the dislocations generated during shock loading in high stacking fault energy materials arrange in ordered cell structures whose size and misorientation angle depend on the applied pressure and pulse time [49]. Since dislocation reorganization into cell structures requires some thermal activation, usually cells become better developed as the strain rate decreases. In low stacking fault energy metals, however, dislocation rearrangement during dynamic deformation is more sluggish and thus homogeneous dislocations distributions develop.

We have observed that significant dislocation rearrangement to form new boundaries subdividing the original grains takes place when the AZ31 alloy is tested both at quasi-static and at dynamic rates (Figs. 2,3,7). However, the misorientation of these geometrically necessary boundaries can reach very high angles in AZ31 exceeding, in some cases, 15°, whereas the typical misorientation of a cell boundary is rarely higher than 1° or 2°. Such highly misoriented geometrically necessary boundaries have been observed only in rare cases, such as when deforming severely (ε=1) pure Al by equal channel angular pressing [64]. It is remarkable that dislocation rearrangement can take place to such an extent at dynamic rates, where thermal activation is very limited. The explanation for this phenomenon might be related to the very high values of the stacking fault energies corresponding to both <c+a> and prismatic $<\bar{1}00>$ dislocations in Mg alloys, which are activated under all the conditions investigated here, as described in the previous sections. These values are compared in Table I to those corresponding to other metals [65-67].

The phenomenon of grain subdivision is most pronounced in the sample deformed quasi-statically in tension along RD, resulting in a large reduction of the grain size with increasing deformation (from 13 μm to 2.5 μm). This can be rationalized as follows. Firstly, the predominant deformation mechanism is the slip of prismatic dislocations, which have a high stacking fault energy [66]. Secondly, prismatic slip predominates during *all* the deformation stages and, thus, carries a large amount of the total strain (not all, as basal slip also takes place to some extent). This is not the case of the compression test along RD, where twinning carries quite a large portion of the strain during the first stages of deformation and pyramidal <c+a> slip, also with a high stacking fault energy [66], becomes predominant only in the latter stages of deformation. This is also not the case if the test carried out in compression along ND, since the total strain to failure is small (0.07). Thirdly, grain subdivision is more pronounced in the test in tension along RD at quasi-static rates than at dynamic rates due to the easier thermal activation in the former case.

5. Conclusions

The microstructural evolution during dynamic deformation (strain rate of ~10^3 s^{-1}) of an AZ31 Mg rolled sheet with a typical basal fiber texture and an equiaxed grain size around 13 μm has been investigated and the following conclusions have been drawn from the present work:

1. $\{10\bar{1}2\}$ extension twin nucleation and propagation are dramatically enhanced at dynamic rates. Contraction and secondary twinning, however, are not favored at such high rates. The choice of $\{10\bar{1}2\}$ twinning at 10^3 s^{-1} may be attributed to the simpler atom shuffles involved.

2. The polarity of twinning may be inverted at dynamic rates. In particular, $\{10\bar{1}2\}$ twinning, which is well known to be an extension twin in the AZ31 alloy, has been observed to take place in grains in which the c-axes are compressed during dynamic compression along the normal direction.

3. Grain subdivision by the formation of geometrically necessary boundaries occurs readily in the AZ31 alloy during both quasi-static and dynamic deformation. Dislocation accumulation and rearrangement takes place with increasing deformation in both strain rate regimes, leading to a gradual increase in the misorientation of the newly formed boundaries, which may eventually become high angle boundaries. The process of grain subdivision is more pronounced at low strain rates due to the easiness of thermal activation, which favors dislocation rearrangement.

4. The extent to which grain subdivision takes place depends on the relative orientation between the applied stress and the c-axes of the crystallites. This phenomenon is most pronounced in the sample tested in tension along RD since prismatic dislocations, which have a high stacking fault energy, carry most of the strain up until failure.

Acknowledgements

The authors would like to thank the vehicle interior manufacturer, Grupo Antolin Ingenieria, S.A., within the framework of the project MAGNO2008-1028-CENIT funded by the Spanish Ministry. Funding from Konauto Manufacturing 0,0 (within the Etortek Programme) is acknowledged. Neutron diffraction measurements were supported by the EC under the sixth FP through the Key Action: Strengthening the ERA, Research Infrastructures, contract no. RII3-CT-2003-505925. The help provided by G. Arruebarrena, U. Garbe, P. Spalthoff, W. Gan and C. Randau is gratefully

acknowledged. Assistance from María Jesús Pérez (UPM, Madrid) and Jesús Reales (CENIM, Madrid) with the mechanical testing and from Yu Kyung Shin and V. Kree (HZG, Germany) with the EBSD analysis was appreciated. The technicians at the CAI Difracción de Rayos X of UCM are acknowledged for their help with the macrotexture measurements. Prof. Daniel Rittel (Technion, Israel) is sincerely thanked for stimulating discussions.

References

[1] Easton M, Beer A, Barnett M, Davies C, Dunlop G, Durandet Y, Blacket S, Hilditch T, Beggs P. JOM 2008;60:57.

[2] Mordike BL, Ebert T. Mater Sci Eng 2001;302:37.

[3] Bamberger M, Dehm G. Annu Rev Mater Res 2008; 38:505.

[4] Couling SL,Pashak JF, Sturkey L. Trans ASM 1959;51:94.

[5] Kocks UF, Westlake DG. Trans AIME 1967;239:1107.

[6] Kelley EW, Hosford WF. Trans AIME 1968;242:654.

[7] Couret A, Caillard D. Acta metal 1985;33:1455.

[8] Chin GY, Mammel WL. Metall Trans 1970;1:357.

[9] Yoo MH. Metall Trans 1981;12A:409.

[10] Vagarali SS, Langdon TG. Acta Metall 1981;29:1969.

[11] Zelin MG, Yang HS, Valiev RZ, Mukherjee AK. Metall Trans 1992;23:3135.

[12] Munroe N, Tan X. Scripta Mater 1997;36:1383.

[13] Agnew SR, Yoo MH, Tomé CN. Acta mater 2001;49:4277.

[14] Watanabe H, Tsutsui H, Mukai T, Kohzu M, Tanabe S, Higashi K. Int J Plasticity 2001;17:387.

[15] Barnett MR. J Light Metals 2001;1:167.

[16] Agnew SR, Tomé CN, Brown DW, Holden TM, Vogel SC. Scripta Mater 2003; 48:1003.

[17] Galiyev A, Sitdikov O, Kaibyshev R. Mater Trans 2003;44:426.

[18] Koike J, Kobayashi T, Mukai T, Watanabe H, Suzuki M, Maruyama K, Higashi K. Acta mater 2003;51:2055.

[19] Barnett MR. Metall Mater Trans 2003;34:1799.

[20] Gehrmann R, Frommert MM, Gottstein G. Mater Sci Eng 2005;395:338.

[21] Barnett MR, Keshavarz Z, Beer AG, Atwell D. Acta Mater 2004; 52:5093.

[22] Agnew SR, Duygulu Ö. Int J Plasticity 2005;21:1161.

[23] Del Valle JA, Pérez-Prado MT, Ruano OA. Metall Mater Trans 2005; 36:1427.

[24] Keshavarz Z, Barnett MR. Scripta mater 2006;55:915.

[25] Meza-García E, Dobroň P, Bohlen J, Letzig D, Chmelik F, Lukáč P, Kainer KU. Mater Sci Eng 2007; 462: 297.

[26] Barnett MR. Mater Sci Eng 2007;464:1.

[27] Del Valle JA, Ruano OA. Acta mater 2007;55:455.

[28] Al-Samman T, Gottstein G. Mater Sci Eng 2008;488:406.

[29] Chino Y, Kimura K, Mabuchi M. Mater Sci Eng 2008;486:481.

[30] Jain A, Duygulu O, Brown DW, Tomé CN, Agnew SR. Mater Sci Eng 2008;486:545.

[31] Hutchinson B, Barnett MR, Ghaderi A, Cizek P, Sabirov I. Int J Mat Res 2009;100:556.

[32] Ball EA, Prangnell PB. Scripta Metall Mater 1994;31:111.

[33] Lou XY, Li M, Boger RK, Agnew SR, Wagoner RH. Int J Plasticity 2007;23:44.

[34] Christian JW, Mahajan S. Prog Mater Sci 1995;39:1.

[35] Barnett MR. Mater Sci Eng 2007:464:8.

[36] Wonsiewizc BC, Backofen WA. Trans AIME 1967; 239:1422.

[37] Hartt WH and Reed-Hill RE. Trans AIME 1968;242:1127.

[38] Hartt WH and Reed-Hill RE. Trans AIME 1968;239:1511.

[39] Nave MD, Barnett MR. Scripta mater 2004;51:881.

[40] Barnett MR, Nave MD, Bettles CJ. Mater Sci Eng 2004;386:205.

[41] Cizek P, Barnett MD. Scripta mater 2008;59:959.

[42] Knezevic M, Levinson A, Harris R, Mishra RK, Doherty RD, Kalidindi SR. Acta mater 2010;58:6230.

[43] Ulacia I, Dudamell NV, Gálvez F, Yi S, Pérez-Prado MT, Hurtado I. Acta Mater 2010;58;2988.

[44] Ishikawa K, Watanabe H, Mukai T. Mat Lett 2005;59:1511.

[45] Ishikawa K, Watanabe H, Mukai T. J Mat Sci 2005;40:1577.

[46] Watanabe H, Ishikawa K, Mukai T. Key Eng Mater 2007;340-341:107.

[47] Watanabe H, Ishikawa K. Mater Sci Eng 2009;523:304.

[48] Ulacia I, Salisbury CP, Hurtado I, Worswick MJ. J Mater Proc Technol, 2009, submitted.

[49] Mtex Software, R. Hielscher, TU Chemnitz, Germany.

[50] Meyers MA. Dynamic Behavior of Materials. New York: John Wiley & Sons; 1994, p.448.

[51] Bai YL, Dodd B. Adiabatic Shear Localization-Occurrence, Theories and Applications. New York: Pergamon; 1992.

[52] Zener C, Hollomon JH. J Appl Phys 1944;15:22.

[53] Rittel D, Landau P, Venkert A. Phys Rev Lett 2008; 101: 165501.

[54] Fernández A, Pérez-Prado MT, Wei Y, Jérusalem A, Int J Plast 2011, submitted.

[55] Kocks UF, Mecking H. Prog Mater Sci 2003;48:171.

[56] Padilla HA, Smith CD, Lambros J, Beaudoin AJ, Robertson IM, Metall Mater Trans 2007; 38A:2916.

[57] Gurao NP, Kapoor R, Suwas S. Acta Materialia 2011;59:3431.

[58] Nemat-Nasser S, Guo WG, Cheng JY. Acta materialia 1999;47:3705.

[59] Jaswon MA, Dove DB. Acta Crystallogr 1956;9:621.

[60] Bilby BA, Crocker AG. Proc Roy Soc 1965;288:240.

[61] Serra A, Bacon DJ. Mater Sci Eng 2005;400-401:496.

[62] Li B, Ma E. Phys Rev Lett 2009;113:035503.

[63] Serra A, Bacon DJ, Pond RC. Phys Rev Lett 2010;104:029603.

[64] Cabibbo M, Blum W, Evangelista E, Kassner ME, Meyers MA. Metall Trans 2008;39:181.

[65] Wen L, Chen P, Tong ZF, Tang BY, Peng LM, Ding WJ. Eur Phys J B 2009;72:397.

[66] Smith AE. Surface Sci 2007;601:5762.

[67] Murr LE. Interfacial Phenomena in Metals and Alloys. Addison-Wesley, Reading MA, 1975.

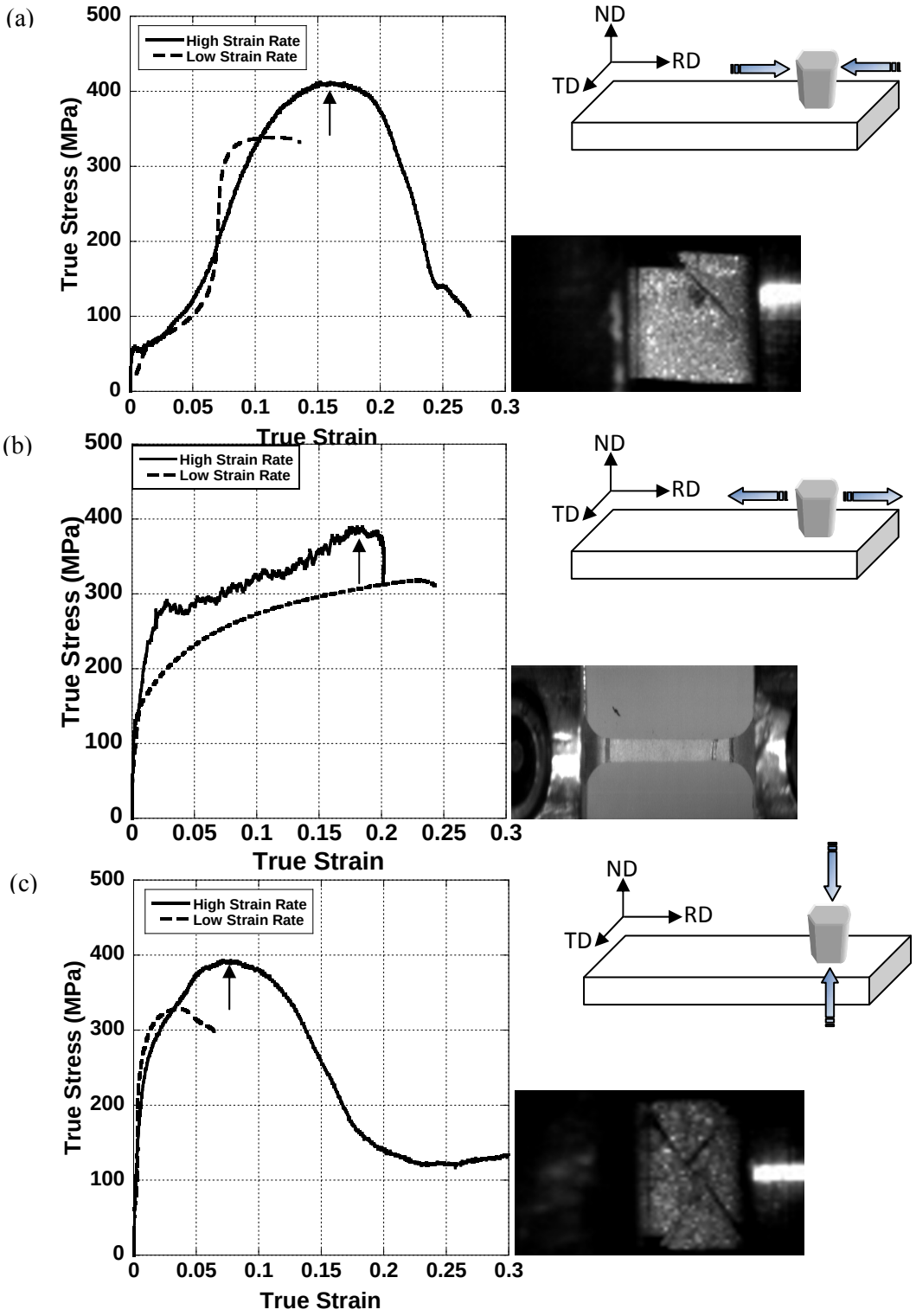

Figure 1. Room temperature stress-strain curves corresponding to the AZ31 alloy deformed at high strain rate (10^3 s^{-1}) and at quasi-static strain rates ($5x10^{-3}$ s^{-1}) in (a) compression along RD; (b) tension along RD; and (c) compression along ND. Images of the specimen after fracture, taken in real time with a high speed camera, are included next to each plot. The strains to failure corresponding to each tests, ε_f, are pointed out with arrows.

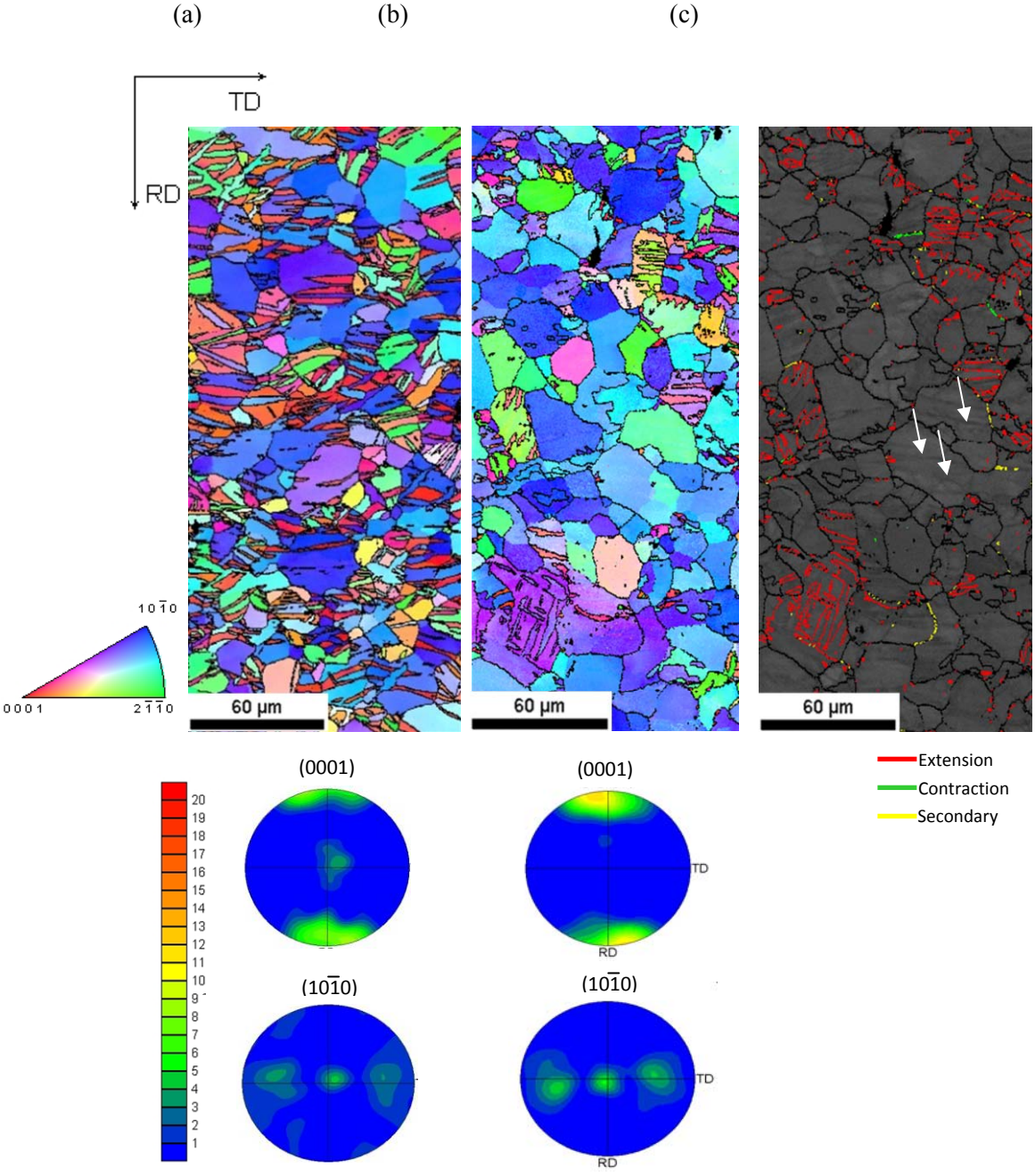

Figure 2. EBSD inverse pole figure maps in the ND and microtextures measured in the samples deformed quasi-statically at room temperature in compression along RD up to strains of (a) 0.05, (b) 0.13. (c) Twin boundary map corresponding to the sample strained up to 0.13. Extension twin boundaries are colored in red, contraction twin boundaries are colored in green and secondary twin boundaries are colored in yellow. White arrows indicate the low and medium angle boundaries formed as a consequence of grain subdivision.

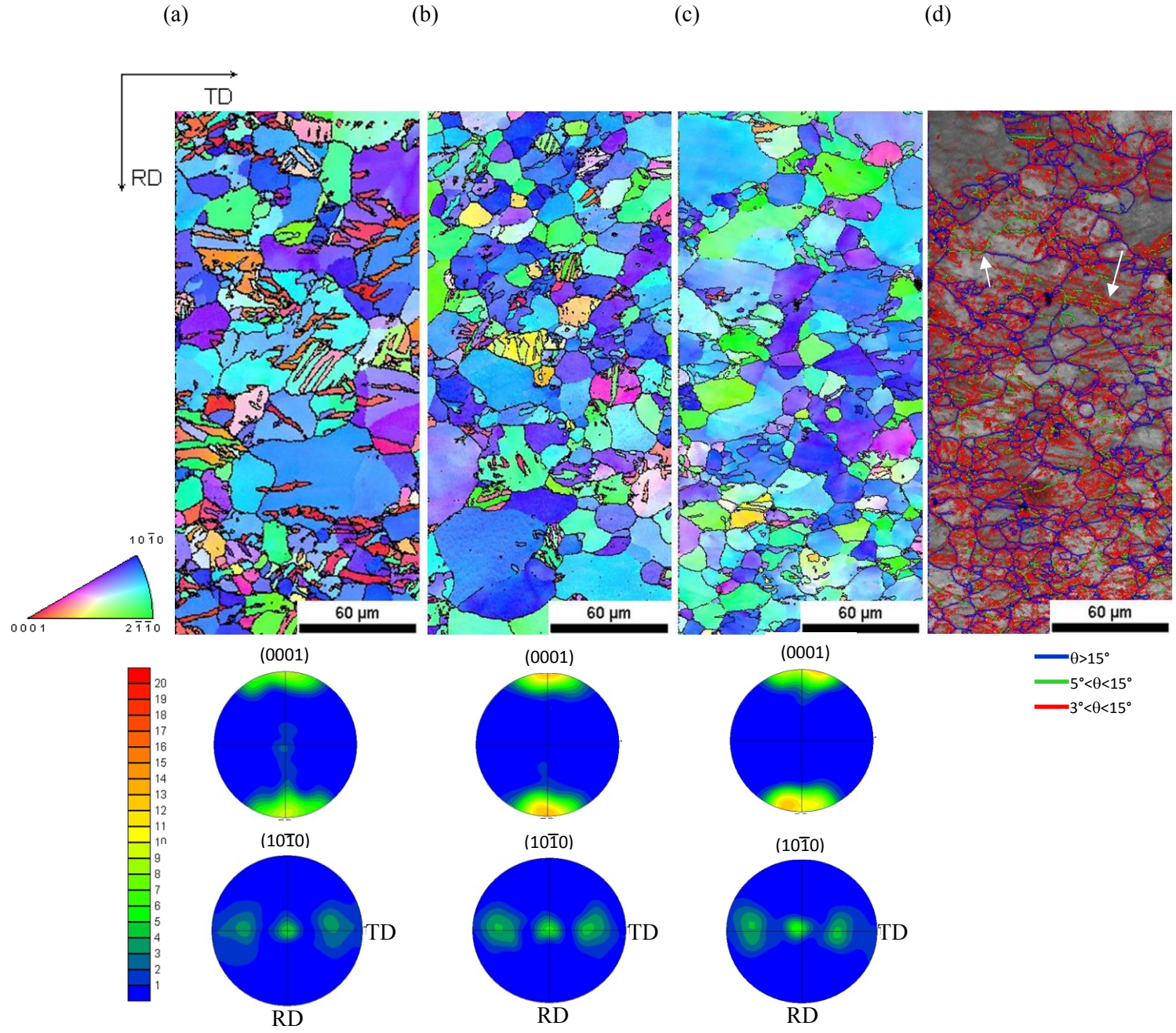

Figure 3. EBSD inverse pole figure maps in the ND and microtextures measured in the samples dynamically loaded at room temperature in compression along RD up to strains of (a) 0.05, (b) 0.10, and (c) 0.13. (d) Boundary map corresponding to the sample strained up to 0.13. High angle boundaries (θ> 15°) are colored in blue, moderately misoriented boundaries (5°<θ<15°) are colored in green and low angle boundaries (3°<θ <5°) are colored in red. White arrows indicate boundaries transitioning from being low to medium angle or from medium to high angle.

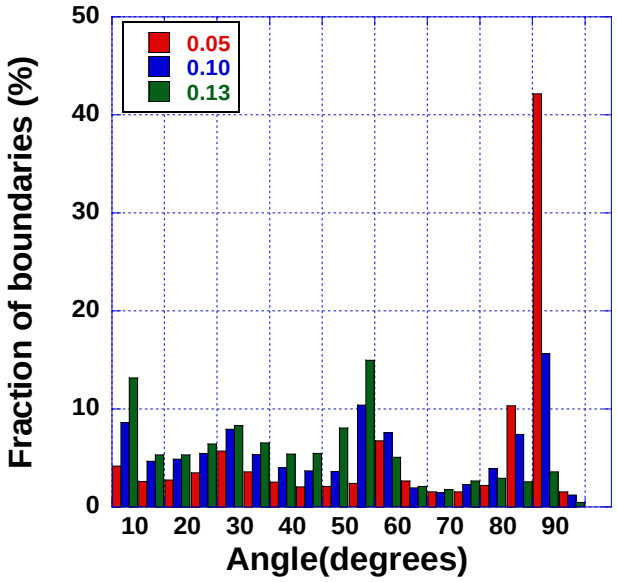

Figure 4. Misorientation distribution histograms corresponding to AZ31 compressed along RD at room temperature up to strains of 0.05, 0.10, and 0.13.

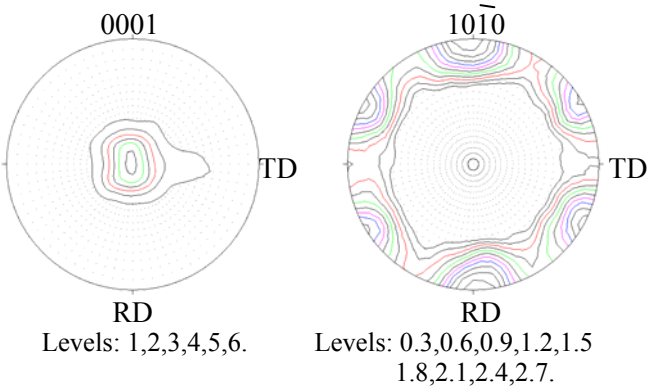

Figure 5. Texture of the AZ31 alloy deformed to failure at room temperature in tension along RD at a strain rate of 10^{-3} s^{-1}. Direct pole figures, measured by neutron diffraction.

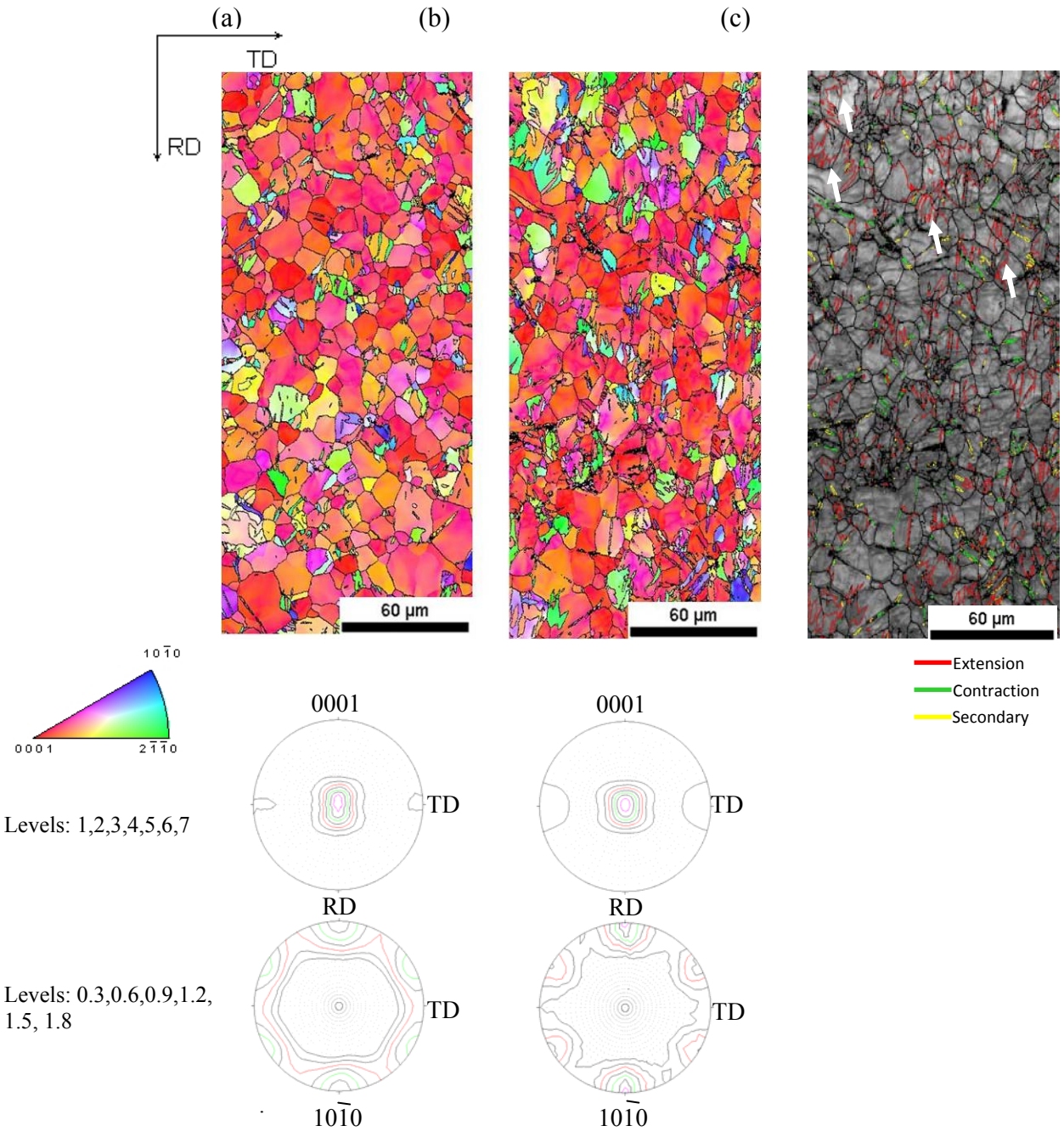

Figure 6. EBSD inverse pole figure maps in the ND and direct pole figures, measured by neutron diffraction, corresponding to the samples dynamically loaded at room temperature in tension along RD up to strains of (a) 0.10, (b) 0.20. (c) Twin boundary map corresponding to the sample deformed to 0.20. Extension twin boundaries are colored in red, contraction twin boundaries are colored in green and secondary twin boundaries are colored in yellow.

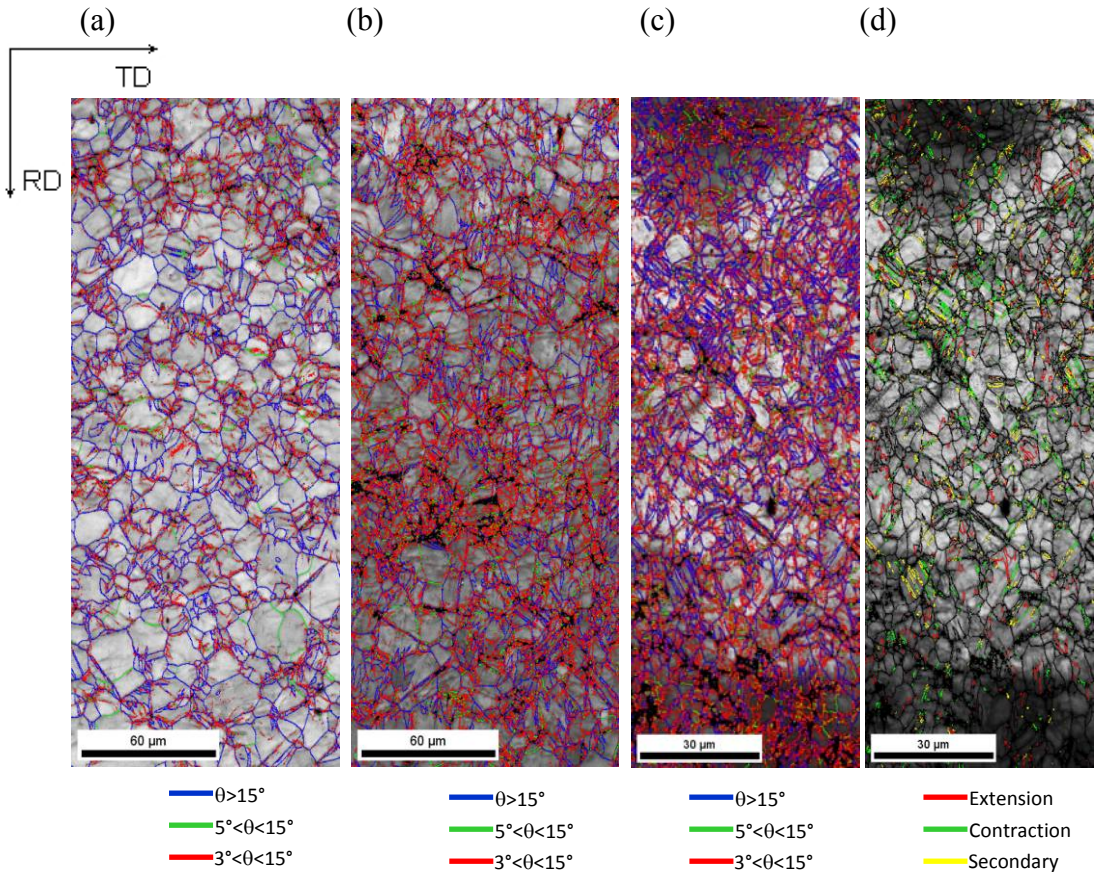

Fig. 7. Boundary maps corresponding to the AZ31 alloy deformed in tension along RD (a) at high strain rate up to a strain of 0.10; (b) at high strain rate up to a strain of 0.20; (c) at low strain rate up to failure (failure strain approximately equal to 0.20). High angle boundaries ($\theta>15°$) are colored in blue, moderately misoriented boundaries ($5°<\theta<15°$) are colored in green and low angle boundaries ($3°<\theta<5°$) are colored in red. (d) Twin boundary map corresponding to the sample deformed at low strain rate until failure. Extension twin boundaries are colored in red, contraction twin boundaries are colored in green and secondary twin boundaries are colored in yellow. Please note that the maps in (c) and (d) are taken at a higher magnification.

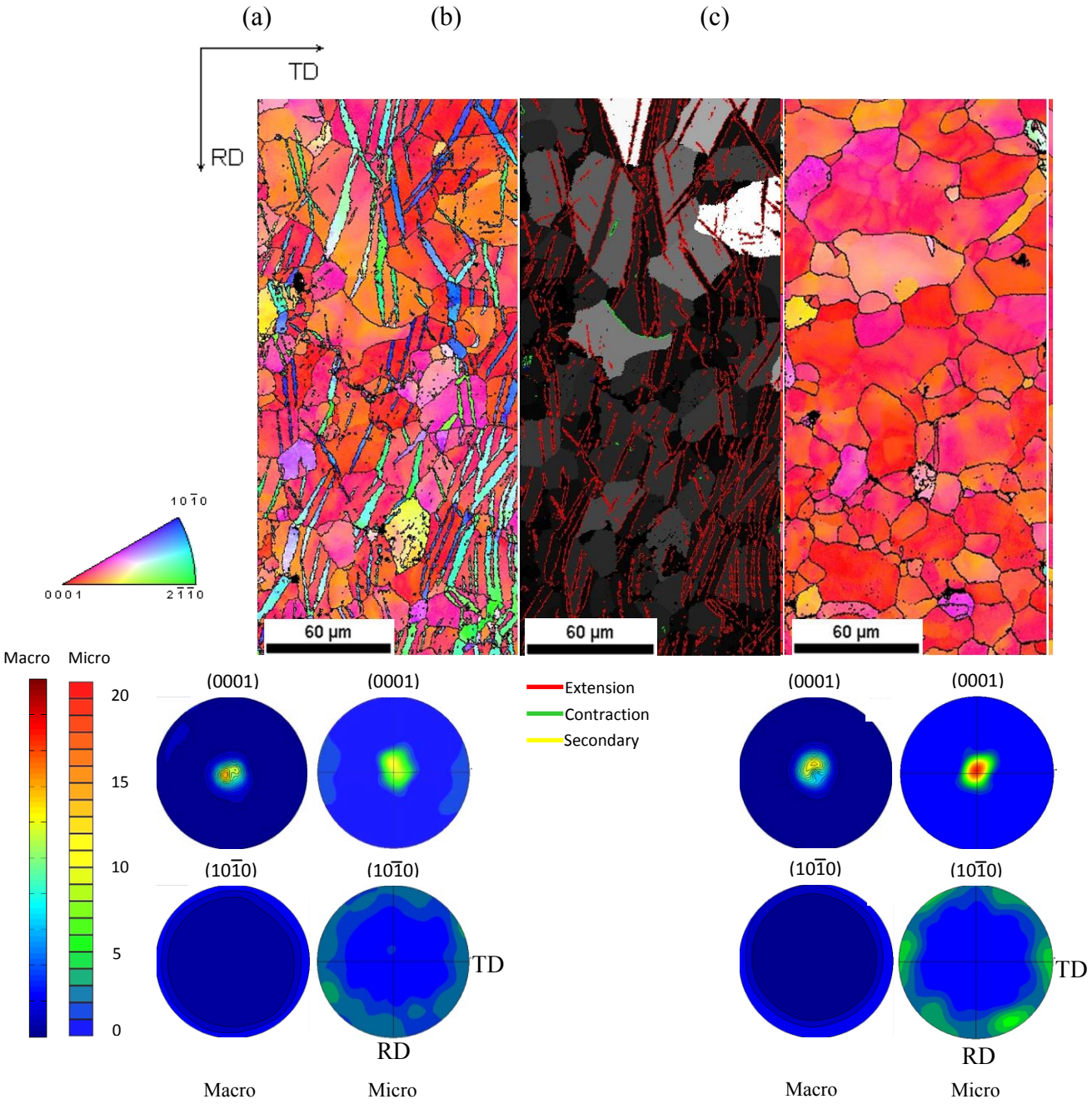

Figure 8. (a) EBSD inverse pole figure map in the ND, macrotexture (X-ray) and microtexture (EBSD) corresponding to the AZ31 alloy dynamically loaded at room temperature in compression along ND up to a strain of 0.05; (b) Twin boundary map corresponding to the same sample (extension twin boundaries are colored in red, contraction twin boundaries are colored in green and secondary twin boundaries are colored in yellow); (c) EBSD inverse pole figure map in the ND, macrotexture (X-ray)

and microtexture (EBSD) corresponding to the AZ31 alloy dynamically loaded at room temperature in compression along ND up to a strain of 0.10.

	Mg-Pyramidal <c+a>	Mg-Prismatic <10-10>	Mg-Basal	Ag	Al	Cu	Ni
γ ($mJ.m^{-2}$)	452 [65]	354 [65] 265 [66]	<50 [66]	22 [67]	200 [67]	78 [67]	128 [67]

Table I. Comparison of the stacking fault energies corresponding to non-basal and basal dislocations in Mg with those of other metals.